(Supplementary Materials)

Red Green Blue Emissive Lead Sulfide Quantum Dots: Heterogeneous Synthesis and Applications

Bo Hou,[a] Yuljae Cho,[a] Byung-Sung Kim,[a] Docheon Ahn,[c] Sanghyo Lee,[a] Jong Bae Park,[b] Young-Woo Lee,[a] John Hong,[a] Hyunsik Im,[d] Stephen M. Morris,[a] Jung Inn Sohn,[a]* SeungNam Cha,[a]* and Jong Min Kim[e]

[a] Department of Engineering Science, University of Oxford, Parks Road, Oxford OX1 3PJ U.K.
[b] Jeonju centre, Korea Basic Science Institute, Jeonju, Jeollabuk-do 54907, Republic of Korea
[c] Beamline Department, Pohang Accelerator Laboratory, Pohang 790-784, Republic of Korea
[d] Division of Physics and Semiconductor Science, Dongguk University, Seoul 100-715, Republic of Korea
[e] Department of Engineering, University of Cambridge, 9 JJ Thomson Avenue, Cambridge CB3 0FA U.K.

*Corresponding authors: junginn.sohn@eng.ox.ac.uk, seungnam.cha@eng.ox.ac.uk

Materials and Methods (SI)

Chemicals

Lead (II) oxide (PbO, 99.999% trace metals basis), sulfur (S, flakes, >99.99% trace metals basis), tetrabutylammonium iodide (TBAI, reagent grade, 98%), 1,2-ethanedithiol (EDT, technical grade, ≥90%), 1-octadecene (ODE, technical grade, 90%), oleic acid (OA, technical grade, 90%), methanol (ACS reagent, ≥99.8%), acetone (CHROMASOLV®, for HPLC, ≥99.8%), ethanol (for HPLC, gradient grade, ≥99.8%), toluene (anhydrous, 99.8%), selenium (99.99% trace metals basis), hexane (CHROMASOLV®, for HPLC, ≥99.8%), zinc stearate (technical grade), zinc acetate dehydrate (ACS reagent, ≥98%), chloroform (anhydrous, ≥99%), and potassium hydroxide (KOH, ACS reagent, ≥85%) were purchased from Sigma-Aldrich and were used without any further purification.

Synthesis and purification of visible emissive PbS QDs.

The Pb precursor was prepared in a two-neck flask, which was loaded with 0.47 g (2.106 mmol) of PbO, 1.49 mL (4.212 mmol) of OA (PbO : OA = 1 : 2) and 20 mL of ODE. The solution was degassed at 100 °C in vacuum for two hours until a clear solution was formed. Then the solution was cooled down to room temperature under Ar. Subsequently, 0.032 g (1 mmol) sulfur flake was added to the solution. The reaction temperature of the flask was elevated at a ramp rate of 0.2°C/s after the addition of sulfur

and different sizes of visible emissive PbS QDs were formed at different temperature (see Table S1). The reaction flask was subsequently left to cool to room temperature using an ice bath after the desired size of QD was formed.

Table S1. A summary of synthesis conditions and optical properties extracted from the as-prepared PbS QDs and other previous reports. Absorption errors are generated from various absorption onset values.

	Absorption (eV)	Emission (eV)	Reaction temperature (°C)	Method	Reference
PbS	1.83 ± 0.06	1.82	170	Heterogeneous reaction	Current work
PbS	2.22 ± 0.12	2.02	170	Heterogeneous reaction	Current work
PbS	2.64 ± 0.22	2.39	190	Heterogeneous reaction	Current work
PbS	3.09 ± 0.16	2.81	200	Heterogeneous reaction	Current work
PbS	2.5	None emission	120	'hot-injection'	[1]
PbS	2.24	None emission	120	'hot-injection'	[1]
PbS	3.54	None emission	50	'Alcohol Injection'	[2]
PbS	2.43	None emission	5	'hot-injection'	[3]
PbS	2.25	None emission	10	'hot-injection'	[3]
PbS	2.07	1.69	25-70	'Non-Injection'	[4]
PbS	1.91	1.6	50	'Alcohol Injection'	[2]
PbS	1.82	1.65	70	'hot-injection'	[3]
PbS	2	1.59	75	'hot-injection'	[5]

10 mL of hexane is added to the cooled solution and centrifugation was carried out at 8000 rpm for the purification. The precipitate was discarded and acetone was added to the supernatant followed by 10 min of 8000 rpm centrifugation. The dispersion in hexane and precipitating with ethanol (1/10, v/v) were carried out two times. 2 mL oleic acid is added into the hexane phase when the precipitate does not dissolve in hexane. After drying the precipitation, the QD was finally dispersed into toluene with a weight concentration of 50 mg/mL for device fabrication and characterization.

Synthesis and purification of ZnS QDs.

The zinc precursor was prepared in a two-neck flask, which was loaded with 1.27 g (2 mmol) of zinc stearate, 1.42 mL (4 mmol) of OA and 20 mL of ODE. The solution was

degassed at 100 °C in vacuum for two hours until a clear solution was formed. Then the solution was cooled down to room temperature under Ar. Subsequently, 0.032 g (1 mmol) sulfur flake was added to the solution. The reaction temperature of the flask was elevated after the addition of sulfur and different sizes of ZnS QDs were formed at different temperatures. The reaction flask was subsequently left to cool to room temperature using an ice bath after the desired size of QD had been formed. 10 mL of hexane was added to the cooled solution and centrifugation was carried out at 8000 rpm. The precipitate was discarded and acetone was added to the supernatant followed by 10 min of 8000 rpm centrifugation. The dispersion in hexane and precipitating with methanol (1/10, v/v) were carried out two times for further purification.

Synthesis and purification of ZnSe QDs.

The zinc precursor was prepared in a two-neck flask, which was loaded with 1.27 g (2 mmol) of zinc stearate, 1.42 mL (4 mmol) of OA and 20 mL of ODE. The solution was degassed at 100 °C in vacuum for two hours until a clear solution was formed. Then the solution was cooled down to room temperature under Ar. Subsequently, 0.078 g (1 mmol) selenium powder was added into the solution. The reaction temperature of the flask was elevated after the addition of selenium and different sizes of ZnSe QDs were formed at different temperatures. The reaction flask was subsequently left to cool to room temperature using ice bath after the desired size of QD had been formed. 10 mL of hexane was added to the cooled solution and centrifugation was carried out at 8000 rpm. The precipitate was discarded and acetone was added to the supernatant followed by 10 min of 8000 rpm centrifugation. The dispersion in hexane and precipitating with methanol (1/10, v/v) was carried out two times for further purification.

Synthesis and purification of ZnO nanoparticles (NPs).

Zinc acetate dehydrate (0.9788 g) was dissolved by 42 mL of methanol in a two-neck flask equipped with glass condenser, and the solution was heated to 60 °C under air. KOH (0.469 g) was dissolved in 22 mL of methanol and added dropwise into the zinc acetate reaction flask over a period of 10 min. After a total reaction time of 90 min, the flask was then cooled to room temperature. The ZnO nanocrystals were purified by three circles of

centrifuging and dispersing in methanol. Final precipitation was dissolved in chloroform at 50 mg/mL.

Transmission microscope (TEM), energy-dispersive X-ray spectroscopy (EDX) and selected area diffraction characterization (SAED).

The size distributions of the visible emissive PbS QDs were analyzed by TEM (JEOL-3000F at 300kV). The histogram of the size deviation was generated from a statistical measurement on 200 particles. EDX and SAED analysis were performed on JEOL-3000F at 300kV and the camera length was 255.8 mm.

FTIR analysis and olefin-S plausible reaction mechanisms (SII)

FTIR spectra are taken by a Varian Excalibur FTS 3500 spectrometer. As shown in the Figure S1a and b, a depletion of olefin moiety can be resolved. A relative plateau (80^{o}C to 150^{o}C) can be seen in Figure S1c, which indicated a non-linear thermal depletion of olefin as a function of reaction temperature. Generally, elemental sulfur exists primarily in the form of S_8 that melts into a clear yellow liquid phase around 120^{o}C. Various molecular weight polymeric sulfur allotropes can be formed through a radical chain reaction by further heating of the liquid sulfur phase above 150^{o}C (e.g. S flakes start to melt around 150^{o}C). Based on previous works, a plausible reaction mechanism of ODE-S is proposed as depicted in scheme 1.[6, 7] Basically, thermal activated S radical reacts with olefin moiety from the ODE and generates alkyl polysulfide and alkylene polysulfide.[7]

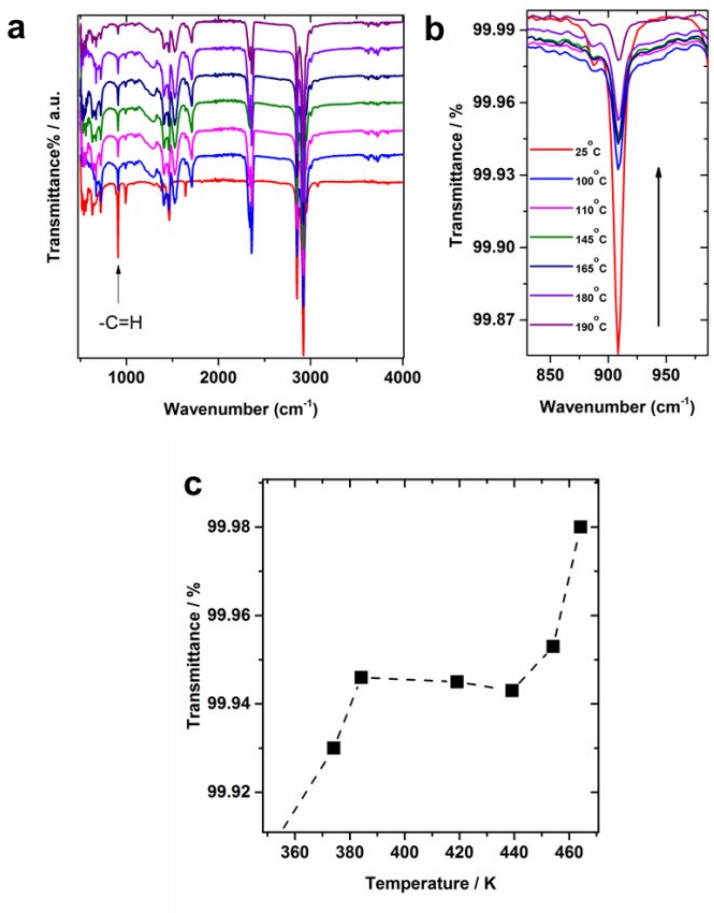

Figure S1. a) Full spectra in-situ FTIR analysis of aliquots taken from the olefin-S reaction. b) Enlarged FTIR spectra which show the characteristic IR peaks related to the olefin moiety. c) Peak transmittances as a function of reaction temperature. Transmittance values are taken from Figure S1b.

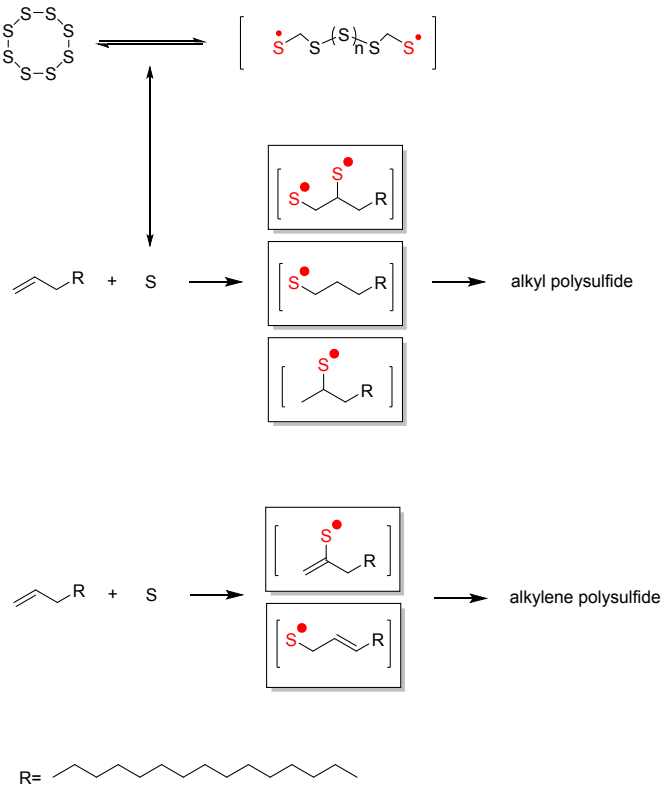

Scheme S1. Plausible mechanisms for the thermally induced olefin-S radical reaction with the generated organosulfur species.[6, 7]

Crystal structure analysis of the visible emissive PbS QDs (SIII)

The ensembles crystal structures are measured using high-resolution powder x-ray diffraction. High-resolution synchrotron powder x-ray diffraction data of the samples were measured at 9B beam line of PLS-II. Remarkably, the bulk cubic phase remains stable even at this dimension (Figure S2). The diffractograms show cubic characteristics, with broad peaks arising from the convolution of (111) and (200) reflections, and with further an identifiable (220) peak. Certainly, ultra-small crystal domains do induce the broad featureless XRD diffractogram and this is consistent with the diffuse ring patterns as revealed in the selected area electron diffraction (SAED) analysis.[8] SAED patterns and HRTEM images of different PL QDs are exemplified in Figure S3 a-j. SAED patterns are quite diffuse in the case of blue and yellow emission QDs, it can just be indexed the (200, 111, 420) reflections from blue PL QDs and (511, 400, 311) reflections from yellow PL QDs. The diffuse SAED ring patterns are improved in the case of red PL QDs and (222, 400, 511) reflections can be indexed. In Figure S3d, HRTEM image (left) and the corresponding inverse Fast Fourier Transform (IFFT, right) contrast enhanced-image of as-prepared Blue PL QDs is presented. The d spacing of 0.34 ± 0.01 nm is typical for cubic phase PbS {111} planes. In Figure S3e, an HRTEM micrograph depicts atomic resolution of as-prepared yellow PL PbS. Right panel image is the IFFT contrast enhanced image. The d spacing of 0.34 ± 0.01 nm is typical for cubic phase PbS {111} planes. In Figure S3f, an HRTEM micrograph depicts atomic resolution of as-prepared red PL PbS. Left image depicts the present of dislocation from the Red PL PbS. d spacing of 0.30 ± 0.01 nm is typical for cubic phase PbS {200} planes and it is exemplified from the right IFFT image. In Figure S3g, the left image depicts some stacking faults from the red PL PbS and a more clear illustration can be found from the right IFFT image. The stacking sequence faulted from ABC to AB and lattice spacing decrease subsequently. d_{200} = 0.29 ± 0.01 nm is also indexed. Figure S3h shows an HRTEM image of as-prepared red PL PbS QDs. The enlarged HRTEM and IFFT contrast enhanced images show a cross-grating pattern of {200} plane with a lattice distance 3.1 ± 0.2 Å (horizontal) and 2.8 ± 0.6 Å (vertical), the intersection angle θ is measured to be 91.4 ± 2.4o. Figure S3i shows an HRTEM image of another red PL QDs. Enlarged HRTEM and IFFT contrast enhanced images show a {200} lattice fringes with a spacing of 3.0 ± 0.2 Å. Figure S3j shows HRTEM image of the dark

red PL QD. The amplified HRTEM and IFFT images show a 3.4 ± 0.1 Å lattice spacing which is indexed to be {111} planes. The PbS QDs also contain dislocations and stacking faults on the {200} planes, as highlighted in FigureS3 g. Consequently, the broadening feature in the XRD and SAED data can be explained to a considerable degree by the structural disorder revealed by the HRTEM.[8] Furthermore, the large Stokes shifts and broad PL peaks may also be linked to these faulted structures (i.e. generating surfaces trap states).

Based on XRD patterns (e.g. 220 diffraction), the crystal domain sizes of as-prepared emissive QDs are also determined by employing the Scherrer equation.[9] In equation 1, d is the size of the crystal domain, k is the shape factor which normally around 0.9, λ denotes the X-ray wavelength (copper kα λ=0.15406nm), β is the line broadening at half the maximum intensity (FWHM, in radians), θ is the Bragg angle (in degrees). The detail parameters and results are listed in Table S2.

$$d = \frac{k\lambda}{\beta \cos\theta} \qquad (1)$$

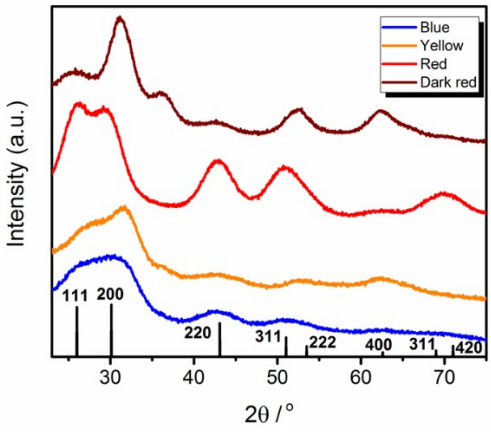

Figure S2. XRD diffractogram of the different size of PbS QDs. The bottom vertical line is cited from PbS standard value PDF=78-1057.

Table S2. A summary of calculation parameters for extracting crystal sizes from XRD data.

QDs	FWHM (radians)	Peak position (220)	θ	Size (nm)
Blue	0.227±0.0010	44.22	22.11	0.66±0.003
Green	0.108±0.00051	44.38	22.19	1.39±0.007
Red	0.096±0.00056	44.17	22.085	1.56±0.009
Dark red	0.064±0.0012	44.99	22.495	2.36±0.046

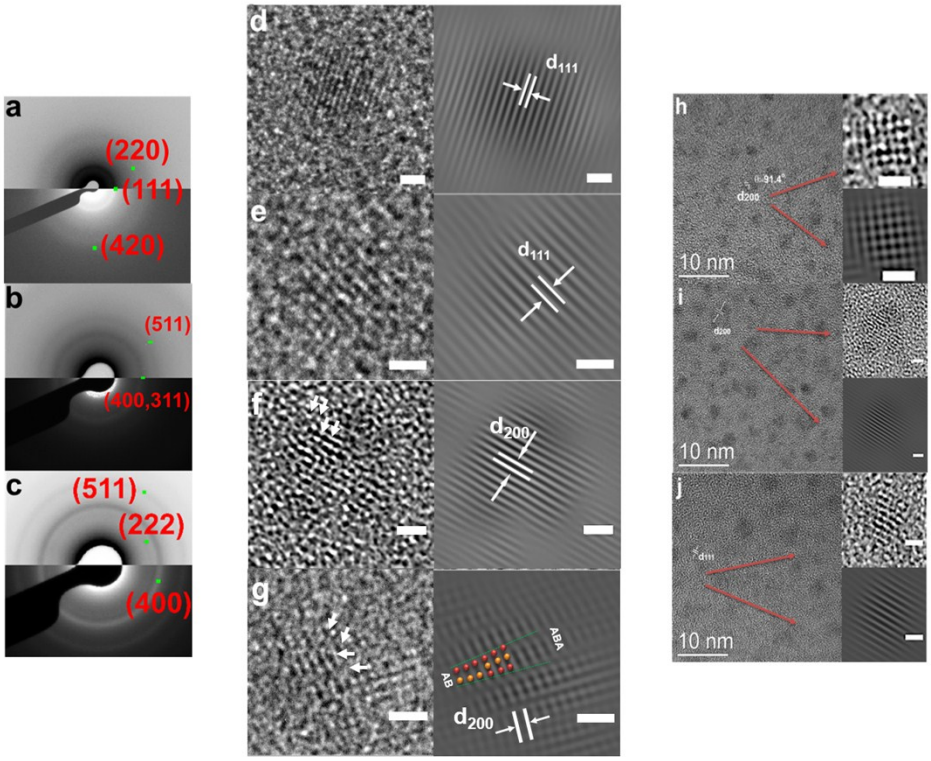

Figure S3 a-c) SAED patterns of the as-prepared blue, yellow and red PL PbS QDs. HRTEM micrographs depict atomic resolution of as-prepared blue d), yellow e), red f-i), dark red j) PL PbS QDs. Scale bars for all these HRTEM and IFFT images are 1 nm.

Composition analysis of the visible emissive PbS QDs (SIV)

Compositions of the visible emissive PbS QDs were characterized by quantized XPS analysis. XPS analysis uses a Thermo Scientific K-Alpha XPS instrument equipped with a micro-focused monochromated Al X-ray source. The source was operated at 12 keV and a 400-micron spot size was used. Normalized atomic percentages are determined from peak areas of the elemental main peaks detected on the survey scan following background subtraction and application of Thermosensitivity factors. The film is prepared by spin coating three layers of QD on top of an ITO slide. As shown in Figure S4, the relative areas of Pb4f to S2s change upon the alternation of QD sizes, but mainly display lead rich features. Table S3 lists the detailed analysis results of the Pb/S ratio with different particle sizes.

Table S3. Quantitated XPS analysis results of the atomic ratio between Pb and S.

QDs	Pb (atomic%)	S (atomic%)	Pb/S ratio
Blue	1.39	1.11	1.25
Green	1.47	1.42	1.04
Red	1.73	1.48	1.17
Dark red	1.79	1.53	1.17

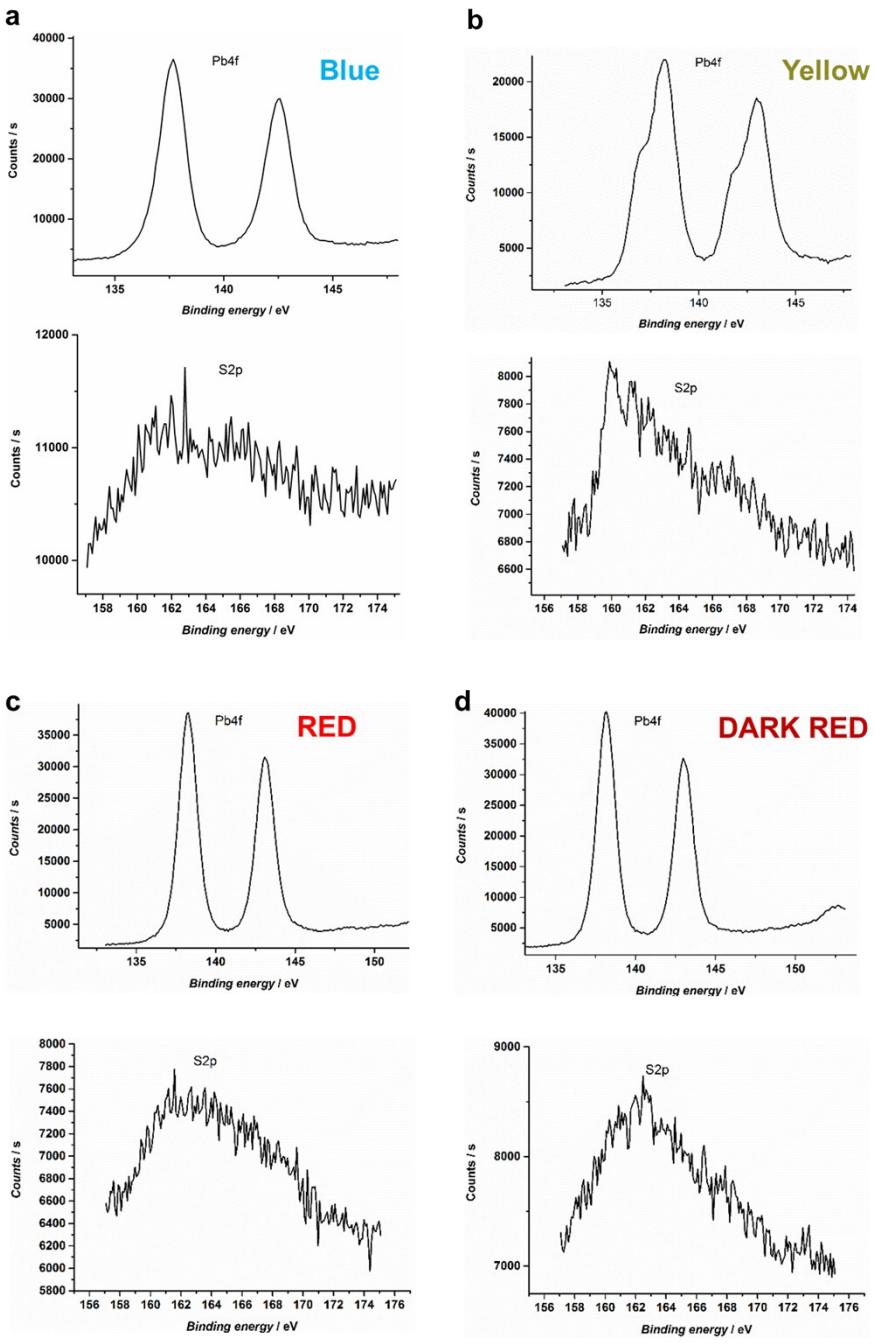

Figure S4. XPS analysis of the visible emissive PbS QDs film on the top of ITO slides. The QDs PL emissions are blue a), yellow b), red c), and dark red d), respectively.

Optical property and monodispersity analysis of visible emissive PbS QDs (SV)

Optical absorption of the visible emissive PbS QDs was analyzed by employing a Cary 5000 UV-vis-NIR spectrometer. The photoluminescence spectra are taken with a Perkin Elmer Luminescence Spectrometer LS55. The typical optical property of the visible emissive PbS QD is demonstrated in Figure S5 through a comparison test with room light (a) and UV 365 nm (b) radiation. Monodispersity of the QDs was evaluated from the FWHM of the PL spectrum and TEM size distribution standard deviation (Std. Dev.). The size distribution and PL data were taken from Figure 1b and Figure 2b in the main text, respectively.

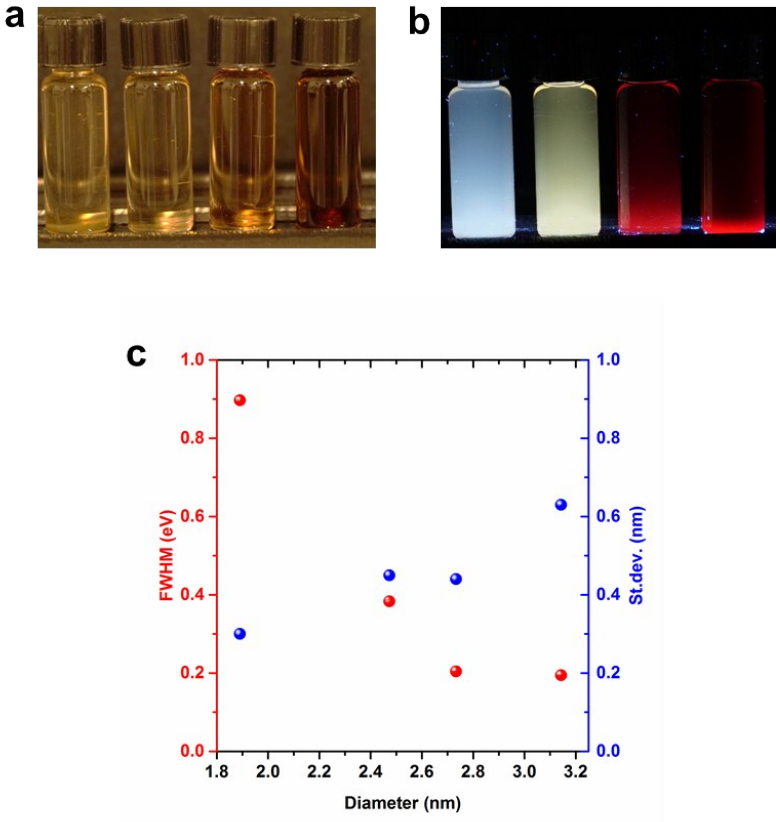

Figure S5. Different sizes of visible emissive PbS QDs dispersed in toluene under room light a) and UV 365 nm exposure b). c) FWHM (red) and TEM size variation results (blue) obtained from the PL spectra and TEM size distribution analysis.

The quantum yields (Φ_{QY}) of PbS QDs fabricated through 'hot-injection' approaches are reported ranging from 5% to 70%.[10] However, the optical band gaps of these QDs only cover NIR range (800-2000nm).[11] In the present work, Rhodamine B (RhB) in absolute

ethanol is employed as a reference for quantum yield (Φ_{QY}) analysis. The absorption and emission spectra of the visible emissive PbS QDs (in toluene), standards Rhodamine B (in ethanol) are measured and displayed in Figure S6. It should be noted that all the solution absorption is controlled below 0.05 to ensure the validation of the measurement and equation 2 is used for the Φ_{QY} calculation. In equation 2, A is the absorbance at the excitation wavelength, PL is the area under the emission curve (expressed in a number of photons), and *n* is the refractive index of the solvents used. Subscripts s and x denote the reference standard and sample, respectively.[12] The detail results are listed in Table S4.

$$\Phi_{QY(x)} = \left(\frac{A_s}{A_x}\right)\left(\frac{PL_x}{PL_s}\right)\left(\frac{n_x}{n_s}\right)^2 \Phi_{QY(s)} \qquad (2)$$

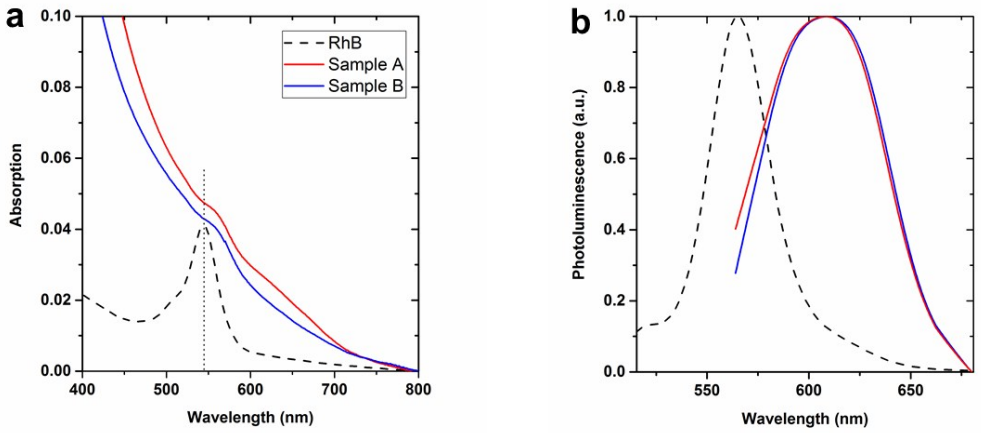

Figure S6. a) Absorption spectra of the visible emissive PbS QDs (solid line) and RhB (dashed line). The vertical dashed line indicates the excitation wavelength used for the PL spectra. b) Emission spectra of the visible emissive PbS QDs (solid line) and RhB (dashed line).

Table S4. Φ_{QY} results and parameters for visible emissive PbS QDs

Substance	Ab ($\lambda_{excitation}$)	PL (area)	n	Φ_{QY}
RhB	0.041	5152.8	1.361	0.49[13]
Sample A	0.047	1758.534	1.498	0.18±0.02
Sample B	0.043	1137.23	1.498	0.125±0.01

Band edge energy levels calculation from UPS analysis (SVI)

Visible emissive PbS QDs coated with different ligands (TBAI or EDT) for UPS measurements were fabricated in air using layer-by-layer spin-coating steps to obtain films (three layers) on ITO substrates. UPS measurements were performed on AXIS – NOVA (KRATOS Inc.) in an ultra-high vacuum chamber with an incident photon source of He (I) (21.2 eV) and a resolution of 0.05 eV. As shown in Figure S7a, the Fermi level is extracted from the difference between incident photon energy of 21.2 eV and high binding energy edge (i.e. 16.89 eV). The energy difference between the valence band edge (ε_v) and the Fermi level (ε_f) is determined from the low binding energy (i.e.0.89 eV). Conduction band edge energy level (ε_c) is calculated from the subtraction of ε_v from band gap (i.e.2.2 eV).[14] The notably large band gap shall be a good candidate for high-performance QDSC, particularly compensating the V_{oc} deficiency. For instance, a 2.3 V direct bandgap semiconductor under 1.5 air mass illuminations, regardless of junction structure, theoretically (thermodynamic limit) can generate up to 2 V V_{oc} at 300 K.[15] Regarding the ligand effects on the energy level alternation, the evolution of the band edge levels as a function of band gap were also studied as shown in Figure S7 b, c. Interestingly, blue PL QDs coated with TBAI shows relatively higher energy level than the EDT coated ones which is uncommon in conventional PbS QDs. Ligand effects previously were considered to result from distinct surface dipole moments arose from Pb-halide anion and the Pb-thiol-carbon interactions.[14] In view of stoichiometry (SIV) of the QD, our visible emissive PbS shows a uniform Pd-rich appearance, which certainly will affect the bonding conditions between the Pb and ligands. We do not exclude the size effect of the dot which holds large surface area compared to the conventional dot. However, we believe that besides of different ligands deduced dipole moments, QD stoichiometry shall also have the influence on the final band edge level variation.

As shown in the inset Figure of Figure S8, photoactive layers consisting of 10 layers of PbS@TBAI and 2 layers of PbS@EDT, together with ZnO/ITO as the cathode and gold as the anode respectively. Flat band potential (ε_{fb}) of ZnO nanoparticles, the work function of ITO (Φ_{ITO}) and gold (Φ_{ITO}) are also characterized by UPS following the same procedure as PbS QDs. The energy levels of the ZnO ε_{fb} and PbS@EDT ε_{VB} (red PL QD) were

estimated to be -3.7 eV and -5.0 eV, respectively. As indexed in the energy diagram, the potential difference (δ_ε) between these two levels was attributed to be the highest V_{oc} this junction structure can produce, which is ca. 1.3 eV.

Table S5 summarized the other reported QD solar cell performance (V_{oc} and PCE) together with our current work. Overall, the PCE values reported herein between 1%~5% (V_{oc}>0.7) motivates future studies. Specifically, we believe that optimizations of the wide band gap PbS QDSC fabrication process can improve the current density and fill factor, which can lead to further improvements in solar cell efficiency.[15-17]

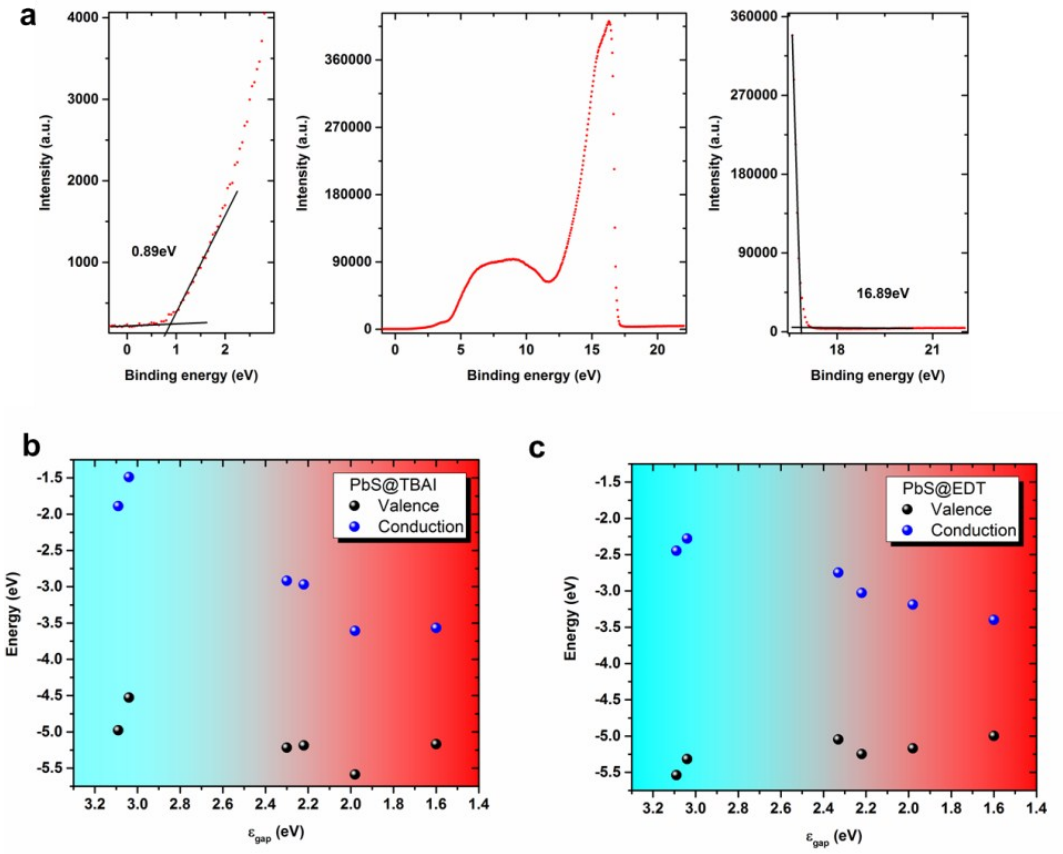

Figure S7. a) Exemplified UPS spectrum for the determination of ε_f and ε_v. ε_v and ε_c energy level evolution as a function of band gaps, the energy level is measured by employing UPS. b) QDs coated with TBAI and c) QDs coated with EDT.

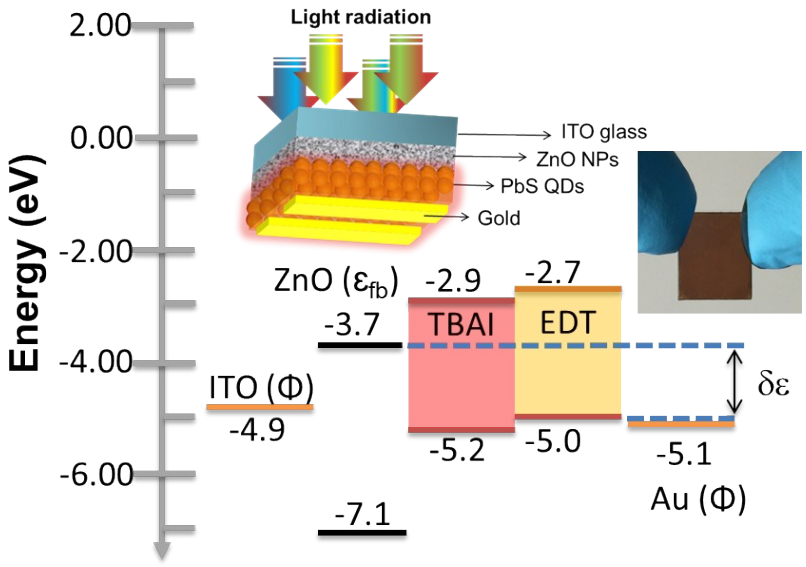

Figure S8. The solar cell operational structure, band alignments, and the Red PL PbS QDs film.

Table S5. V_{oc} and PCE performance data from the as-prepared visible fluorescent PbS QDSC devices under AM 1.5 illuminations. 2.22 eV band gap QDSC results are averaged across 9 samples on 3 different substrates. 1.83 eV band gap QDSC results are averaged across 15 samples on 5 different substrates. V_{oc} and PCE of champion devices are quoted in brackets. The reported V_{oc} and PCE performance data from the other QDs are also cited in the table.

QD	Bandgap(eV)	V_{oc} (V)	PCE (%)	Structure	Reference
PbS	2.22	0.78±0.02 (0.8)	1.2±0.5 (1.82)	ZnO/PbS (solid state)	Current work
PbS	1.83	0.71±0.01 (0.72)	4.61±0.1 (4.69)	ZnO/PbS (solid state)	Current work
PbS	1.37	0.639	9.9	ZnO/PbS (Molecular halides treatment, solid state)	[18]
PbS	1.4	0.69	1.4±0.1	ITO/PbS/LiF/Al (solid state)	[15]
ZnTe@ZnSe	2.48@3.3	0.38	0.0063	P3HT/ZnTe@ZnSe	[19]
ZnSe	3.3	0.27	0.0056	P3HT/ZnSe	[19]
ZnS	3.65	0.57	2.72	ITO/ZnO/ZnS/P3HT&PCBM/Ag	[20]
CdSe	2.25	0.9	0.34	FTO/TiO_2/CdSe 3,3'''-didodecyl-quaterthiophene/ polytriphenylamine/FTO	[21]
CdS	2.4	0.66	0.1	FTO/TiO_2/CdS/spiro-OMeTAD/Ag	[22, 23]
CdTe/$CdSe_{0.2}Te_{0.8}$	1.5/1.4	0.64	7.0	ITO/CdTe/$CdSe_{0.2}Te_{0.8}$/ZnO/Al	[23, 24]
CdTe/CdSe	1.5/1.75	0.19	0.7	ITO/CdTe/CdSe/ZnO/Al	[23, 24]
CdTe	1.5	0.61	7.3	ITO/CdTe/CdTe/ZnO/Al	[23, 24]
$CuInS_3$	2	0.7	1.16	FTO/TiO_2/$CuInS_3$/Au	[25]

J-V curve and EQE spectra analysis of the QDSC (SVII)

In Figure S9, full-spectrum (350 nm-1500 nm) external quantum efficiency (EQE) analysis was carried out on the visible emissive QDSCs. A clear red shift can be observed from the onset of the spectra. It also can be revealed that smaller effective band gaps induced higher EQE. Besides the other composite absorption (i.e. ITO, ZnO etc.) and light reflections, the QDSC exhibits high EQE performance and peaks at 400 nm wavelengths.

Figure S10a shows enlarged plots of Figure 3b (main text) to highlight the V_{oc} improvement. Figure 10b and Figure 10c show another two examples of 2.22eV PbS QDSCs. The devices performances are listed in the images. Figure S10d and Figure S10e show comparisons of current densities extracted from 2.22eV PbS QDSC with 0.8V V_{oc}. The J_{SC} values which are calculated by integrating the EQE spectra with the AM1.5G solar spectrum shows good agreement with the measured J_{SC}.

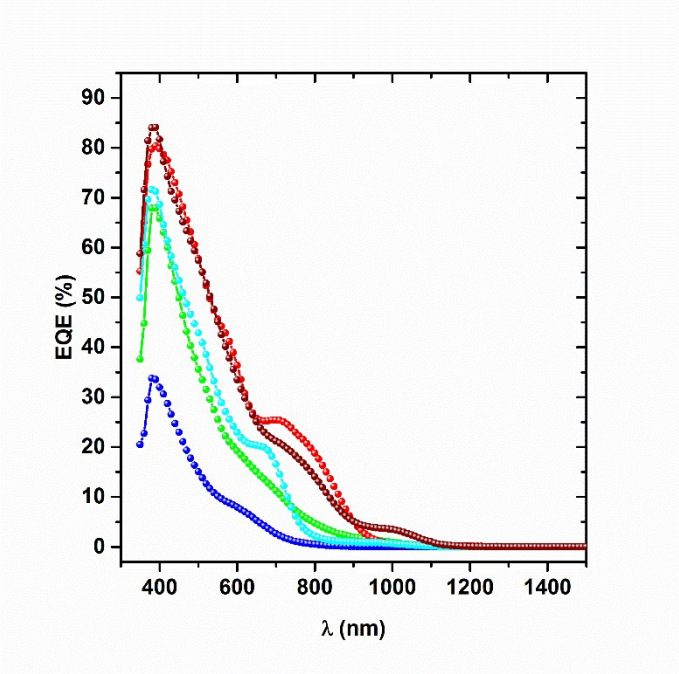

Figure S9. Full-spectra EQE spectra of the QDSCs made from these visible emissive PbS QDs.

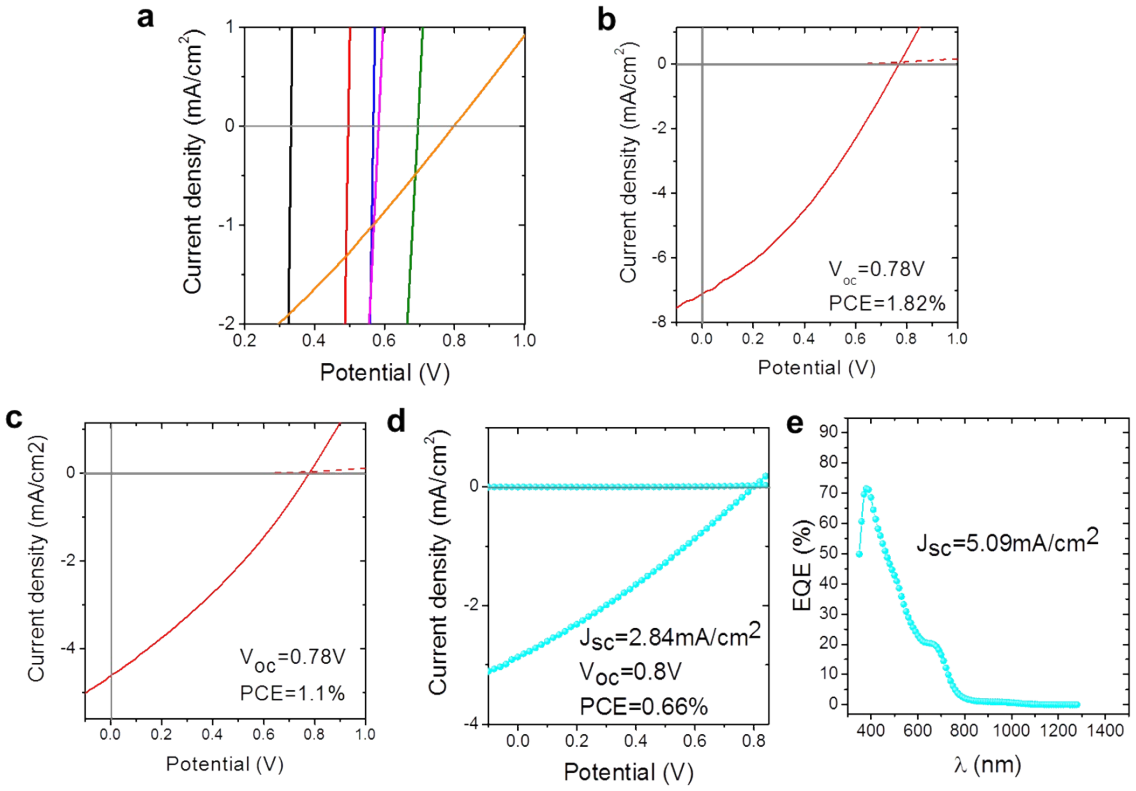

Figure S10. a) Enlarge image of Figure 3b (main text) for highlighting V_{oc} improvement. b) and c) are represented J-V curves from 2.22 eV PbS QDSCs under dark (dashed line) and 1.5AM illumination (solid line). d) and e) are current density verification between EQE spectra integration and as-measured J_{sc} values. J-V and EQE curves for 2.22 eV (blue symbol) PbS QDSCs are provided. EQE spectra are integrated under AM 1.5 G TILT (ASTM-G173-03) with solar cell mask area of 0.012 cm^2.

Characterization of the ZnS and ZnSe QDs (SVIII)

The typical optical properties of the ZnSe and ZnS QDs are demonstrated in Figure S11 and Figure S12. Comparison tests under ambient light and UV 365 nm radiation are provided along with absorption spectra. Crystal structure, size distribution and composition verification are also analyzed through TEM, EDX, and SAED respectively which are presented in Figure S13, Figure S14 and summarized in Table S6.

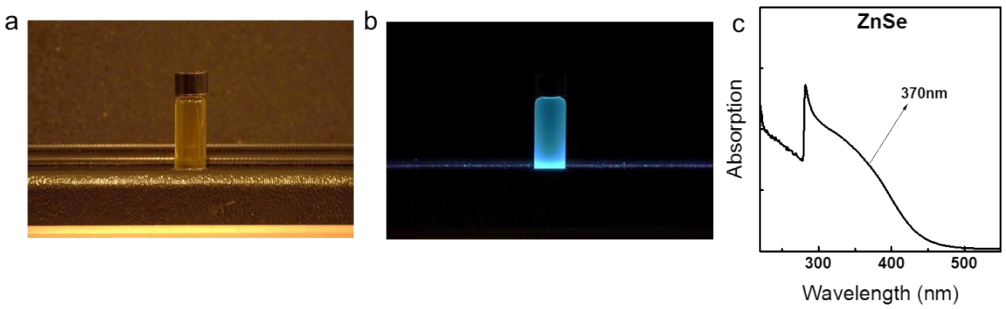

Figure S11. The ZnSe QDs dispersed in toluene under ambient light a) and UV 365 nm exposure b). c) The absorption spectrum of as-prepared ZnSe QDs.

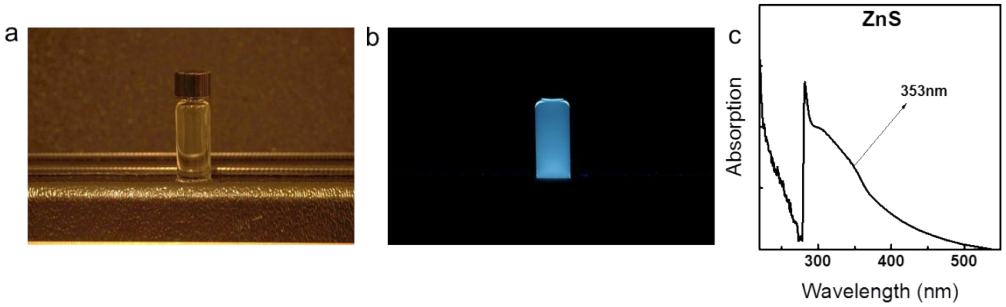

Figure S12. As-prepared ZnS QDs dispersed in toluene under ambient light a) and UV 365 nm exposure b). c) Absorption spectrum of as-prepared ZnS QDs.

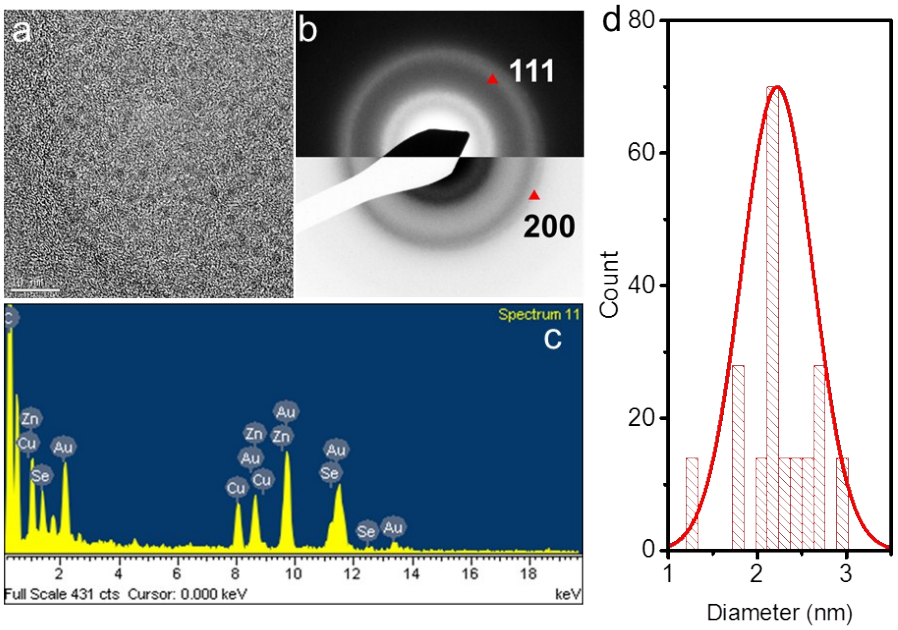

Figure S13. TEM a), enlarged SAED b), EDX c) size distribution d) analysis of the blue PL ZnSe QDs. Scale bar in the TEM equal to 10 nm.

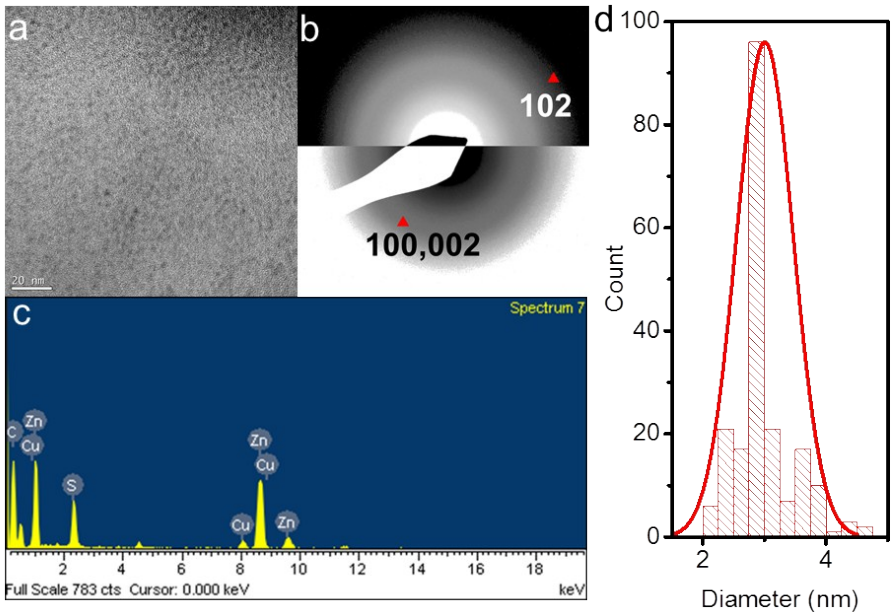

Figure S14. TEM a), enlarged SAED b), EDX c) and size distribution d) analysis of the blue PL ZnS QDs. Scale bar in the TEM equal to 20 nm.

Table S6. Elemental atomic ratios, lattice parameters and size distribution of ZnSe and ZnS QDs extracted from EDX spectra, SAED patterns, and TEM statics analysis. EDX element ratio is an average value from 5 different random regions' analysis.

	EDX (atomic ratio)	**SAED (Å)**	**Size (nm)**	**Lattice constant (Å)**
ZnSe QDs	Zn:Se=2.49 ± 0.5	(111) 3.19 ± 0.1 (200) 2.78 ± 0.1	2.22 ± 0.4	*a*: 5.55 ± 0.1
ZnS QDs	Zn:S=1.86 ± 0.2	(100) & (002) 3.17 ± 0.1 (102) 2.2 ± 0.1	3.01 ± 0.5	*a*: 3.60 ± 0.1 *c*: 6.24 ± 0.1
ZnSe bulk (cubic) PDF= 80-0021		(111) 3.243 (200) 2.809		*a*: 5.618
ZnSe bulk (hexagonal) PDF=80-0008		(100) 3.441 (002) 3.253 (101) 3.042 (102) 2.364		*a*: 3.974 *c*: 6.506
ZnS bulk (cubic) PDF=80-0020		(111) 3.085 (200) 2.672 (220) 1.889		
ZnS bulk (hexagonal) PDF=80-0007		(100) 3.271 (002) 3.094 (101) 2.891 (102) 2.247		*a*: 3.777 *c*: 6.188

Reference

1. E. M. Miller, D. M. Kroupa, J. Zhang, P. Schulz, A. R. Marshall, A. Kahn, S. Lany, J. M. Luther, M. C. Beard, C. L. Perkins and J. van de Lagemaat, *ACS Nano*, 2016, **10**, 3302.
2. A. Antanovich, A. Prudnikau and M. Artemyev, *J. Phys. Chem. C*, 2014, **118**, 21104.
3. A. Shrestha, N. A. Spooner, S. Z. Qiao and S. Dai, *Phys. Chem. Chem. Phys.*, 2016, **18**, 14055.
4. T.-Y. Liu, M. Li, J. Ouyang, M. B. Zaman, R. Wang, X. Wu, C.-S. Yeh, Q. Lin, B. Yang and K. Yu, *J. Phys. Chem. C*, 2009, **113**, 2301.
5. N. Reilly, M. Wehrung, R. A. O'Dell and L. Sun, *Mater. Chem. Phys.*, 2014, **147**, 1.
6. B. Hou, D. Benito-Alifonso, R. Webster, D. Cherns, M. C. Galan and D. J. Fermin, *J. Mater. Chem. A*, 2014, **2**, 6879.
7. W. J. Chung, J. J. Griebel, E. T. Kim, H. Yoon, A. G. Simmonds, H. J. Ji, P. T. Dirlam, R. S. Glass, J. J. Wie, N. A. Nguyen, B. W. Guralnick, J. Park, SomogyiÁrpád, P. Theato, M. E. Mackay, Y.-E. Sung, K. Char and J. Pyun, *Nat Chem*, 2013, **5**, 518.
8. B. Hou, D. Parker, G. P. Kissling, J. A. Jones, D. Cherns and D. J. Fermín, *J. Phys. Chem. C*, 2013, **117**, 6814.
9. A. L. Patterson, *Physical Review*, 1939, **56**, 978.
10. M. Greben, A. Fucikova and J. Valenta, *Journal of Applied Physics*, 2015, **117**, 144306.
11. U. Resch-Genger, M. Grabolle, S. Cavaliere-Jaricot, R. Nitschke and T. Nann, *Nat Meth*, 2008, **5**, 763.
12. G. A. Crosby and J. N. Demas, *J. Phys. Chem.*, 1971, **75**, 991.
13. K. G. Casey and E. L. Quitevis, *J. Phys. Chem.*, 1988, **92**, 6590.
14. C.-H. M. Chuang, P. R. Brown, V. Bulović and M. G. Bawendi, *Nat Mater*, 2014, **13**, 796.
15. W. Yoon, J. E. Boercker, M. P. Lumb, D. Placencia, E. E. Foos and J. G. Tischler, *Sci. Rep.*, 2013, **3**, 2225.
16. G. Nair, L.-Y. Chang, S. M. Geyer and M. G. Bawendi, *Nano Lett.*, 2011, **11**, 2145.
17. W. Ma, S. L. Swisher, T. Ewers, J. Engel, V. E. Ferry, H. A. Atwater and A. P. Alivisatos, *ACS Nano*, 2011, **5**, 8140.
18. X. Lan, O. Voznyy, A. Kiani, F. P. García de Arquer, A. S. Abbas, G.-H. Kim, M. Liu, Z. Yang, G. Walters, J. Xu, M. Yuan, Z. Ning, F. Fan, P. Kanjanaboos, I. Kramer, D. Zhitomirsky, P. Lee, A. Perelgut, S. Hoogland and E. H. Sargent, *Adv. Mater.*, 2016, **28**, 299.
19. J. Bang, J. Park, J. H. Lee, N. Won, J. Nam, J. Lim, B. Y. Chang, H. J. Lee, B. Chon, J. Shin, J. B. Park, J. H. Choi, K. Cho, S. M. Park, T. Joo and S. Kim, *Chem. Mater.*, 2010, **22**, 233.
20. M. Mehrabian, K. Mirabbaszadeh and H. Afarideh, *Phys. Scr.*, 2014, **89**, 085801.
21. I. Barcelo, J. M. Campina, T. Lana-Villarreal and R. Gomez, *Phys. Chem. Chem. Phys.*, 2012, **14**, 5801.

22. T. P. Brennan, P. Ardalan, H.-B.-R. Lee, J. R. Bakke, I. K. Ding, M. D. McGehee and S. F. Bent, *Adv. Energy Mater.*, 2011, **1**, 1169.
23. J. H. Rhee, C.-C. Chung and E. W.-G. Diau, *NPG Asia Mater*, 2013, **5**, e68.
24. B. I. MacDonald, A. Martucci, S. Rubanov, S. E. Watkins, P. Mulvaney and J. J. Jasieniak, *ACS Nano*, 2012, **6**, 5995.
25. D. So, S. Pradhan and G. Konstantatos, *Nanoscale*, 2016, **8**, 16776.